Heart failure drug changes the mechanoenzymology of the cardiac myosin powerstroke

John A. Rohde[a], David D. Thomas[a,1,2], and Joseph M. Muretta[a,1,2]

[a]Department of Biochemistry, Molecular Biology, and Biophysics, University of Minnesota, Minneapolis, MN 55455

Edited by James A. Spudich, Stanford University School of Medicine, Stanford, CA, and approved January 20, 2017 (received for review July 15, 2016)

Omecamtiv mecarbil (OM), a putative heart failure therapeutic, increases cardiac contractility. We hypothesize that it does this by changing the structural kinetics of the myosin powerstroke. We tested this directly by performing transient time-resolved FRET on a ventricular cardiac myosin biosensor. Our results demonstrate that OM stabilizes myosin's prepowerstroke structural state, supporting previous measurements showing that the drug shifts the equilibrium constant for myosin-catalyzed ATP hydrolysis toward the posthydrolysis biochemical state. OM slowed the actin-induced powerstroke, despite a twofold increase in the rate constant for actin-activated phosphate release, the biochemical step in myosin's ATPase cycle associated with force generation and the conversion of chemical energy into mechanical work. We conclude that OM alters the energetics of cardiac myosin's mechanical cycle, causing the powerstroke to occur after myosin weakly binds to actin and releases phosphate. We discuss the physiological implications for these changes.

heart failure | omecamtiv mecarbil | FRET | myosin | phosphate release

Heart failure is the leading cause of mortality in the United States (1). A primary defect in heart failure is a loss in cardiac contractility (2) resulting from a range of molecular factors: the sarcoplasmic reticulum's inability to sequester Ca^{2+}, dysfunction of excitation–contraction coupling, altered metabolism, changes in gene expression levels, and mutations in sarcomeric proteins (3). Treatments for heart failure include lifestyle changes, surgeries, medical devices, heart transplant, renin-angiotensin and β-adrenergic modulators, and inotropes that increase contractility. Despite these interventions, life expectancy remains low, and half of the patients diagnosed with heart failure die within 5 y (1).

Omecamtiv mecarbil (OM) is a small-molecule β-cardiac myosin effector in clinical trials for the treatment of systolic heart failure. OM was developed from lead compounds identified in a high-throughput calcium-regulated and thin-filament-activated ventricular cardiac myosin ATPase activity screen (4). A high-resolution X-ray crystal structure (5) and a photoreactive cross-linking study (4) both suggest that OM binds near the interface of several of myosin's key conserved structural elements: the seven-stranded β-sheet, the C terminus of the relay helix, the SH1 helix, and the interface between the N-terminal and converter domains. Movements in these elements are coupled to the weak-to-strong actin-binding transition, rotation of the myosin light chain domain, actin-induced phosphate and ADP release, and subsequently to force generation (6). Despite a number of recent studies, however (4, 5, 7–11), the structural basis for how OM alters force generation in the heart remains enigmatic.

Mechanically active myosins all use changes in the Gibbs free energy associated with myosin binding to actin, ATP, ADP, and inorganic phosphate (P_i) to drive force-generating structural transitions, most notably a lever arm rotation of the light chain domain (LCD). This rotation, termed the powerstroke, converts the free energy liberated from ATP hydrolysis under non-equilibrium cellular conditions into mechanical work (11, 12). The powerstroke is coupled to actin-activated release of hydrolyzed phosphate, ADP release, and myosin's weak-to-strong actin-binding transition. Structural changes in the myosin nucleotide-binding pocket following actin binding are hypothesized to initiate these transitions and thus initiate force generation (11, 12). OM accelerates phosphate release from the nucleotide-binding pocket (4, 10), and because LCD rotation is coupled to phosphate release, we hypothesized that OM should also accelerate LCD rotation and initiation of the powerstroke.

We tested this hypothesis using transient time-resolved FRET [$(TR)^2$FRET] and transient biochemical kinetics. $(TR)^2$FRET uses subnanosecond time-resolved fluorescence, measured repeatedly and with high signal-to-noise, every 0.1–0.2 ms, during the transient phase of a biochemical rapid-mixing experiment (12, 13). The resulting time-resolved fluorescence waveforms, 10,000–5,000 per s, are independently fit by a structure-based model, revealing the pre–steady-state distribution of nanosecond-resolved structural states detected by FRET and thus how these states evolve over time during the biochemical transient. This approach has revealed the structural kinetics of the recovery stroke of *Dictyostelium discoideum* myosin II (12), the powerstroke and its coordination with phosphate release in both *Dictyostelium discoideum* myosin II (13) and fast skeletal muscle myosin II (14), the recovery and powerstroke in mouse myosin V (15), and the structural kinetics of kinesin family members (16, 17). Here we apply this technology to answer an important question in molecular cardiology: does OM accelerate the actin-activated powerstroke, as suggested by its effect on phosphate release?

Strikingly, our results disproved our initial hypothesis: although OM binding stabilizes the prepowerstroke structural state of cardiac myosin—consistent with kinetic studies (10)—it simultaneously causes the powerstroke to occur more than 10 ms after dissociation of ATP's hydrolyzed phosphate. This inhibition

Significance

Heart failure is the leading cause of mortality in the United States, despite sustained efforts to develop effective small-molecule treatments. The biophysical characterization of existing therapies will drive development of next-generation approaches for treating heart failure. Furthermore, small molecules can be powerful probes for dissecting protein structure function relationships. We used an innovative FRET-based spectroscopic approach to determine that the small-molecule heart disease therapeutic omecamtiv mecarbil (OM) changes how myosin's working powerstroke is coordinated with actin-activated phosphate release, the biochemical step associated with force generation. This result explains how OM alters cardiac contractility at the molecular level, forcing the accumulation of actin-bound prepowerstroke cross-bridges.

Author contributions: J.A.R., D.D.T., and J.M.M. designed research; J.A.R. and J.M.M. performed research; J.A.R. and J.M.M. analyzed data; and J.A.R., D.D.T., and J.M.M. wrote the paper.

The authors declare no conflict of interest.

This article is a PNAS Direct Submission.

[1]D.D.T. and J.M.M. contributed equally to this work.

[2]To whom correspondence may be addressed. Email: muret003@umn.edu or ddt@umn.edu.

This article contains supporting information online at www.pnas.org/lookup/suppl/doi:10.1073/pnas.1611698114/-/DCSupplemental.

suggests the accumulation of an actin-bound structural state of myosin that does not undergo a normal powerstroke. We discuss these effects in detail below.

Results

Time-Resolved FRET Detects ADP- and ATP-Sensitive Structural States of Cardiac Myosin. We used time-resolved FRET (18) and transient time-resolved FRET (12, 13) to determine if OM changes the orientation of the ventricular cardiac myosin LCD in the absence of actin. Previous kinetics studies on porcine ventricular cardiac myosin showed that OM shifts the apparent equilibrium constant for ATP hydrolysis toward the posthydrolysis ADP.P_i biochemical state (10). The orientation of the myosin LCD is coupled to hydrolysis, so OM should alter LCD orientation. To test this hypothesis, we first developed a time-resolved FRET (TR-FRET)-based assay to measure LCD orientation in ventricular myosin. Our previous work inspired this assay (14): we attached the fluorescent donor Alexa Fluor 488 (AF488) to the myosin regulatory light chain domain and then incubated the labeled myosin with fluorescent nucleotides 2′/3′-O-(2-aminoethyl-carbamoyl)-adenosine-5′-tri/di-phosphate (Cy3-ATP, Cy3-ADP, or Cy3-ADP with vanadate).

We prepared the AF488-labeled bovine ventricular cardiac HMM as described in *SI Methods*. The donor AF488 probe, attached to the C-lobe of an exchanged RLC in the HMM, exhibited normal ATPase activity (Fig. S1). The spectral overlap between the AF488 donor and Cy3 acceptor gives a Förster distance (R_0) of 6.7 nm (14), and based on high-resolution crystal structure models of prepowerstroke and postpowerstroke structural states [examples shown in Fig. 1*A*; postpowerstroke, Protein Data Bank (PDB): 1B7D, prepowerstroke, 1DFL], we predicted that the distance between the C-lobe of the RLC and the Cy3-labeled nucleotide ribose would change with LCD rotation and this change would detect the powerstroke. We used a single-cysteine recombinant chicken gizzard RLC, highly homologous to bovine RLC, for these studies because it contains a single cysteine for labeling and can be exchanged efficiently onto the bovine heavy chain under mild conditions that preserve ATPase activity (Fig. S1), summarized in Table S1.

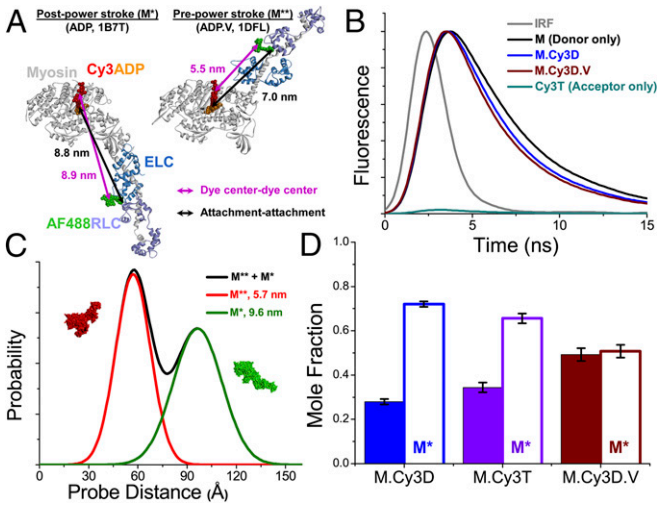

Fig. 1. Time-resolved FRET detects nucleotide-dependent LCD orientation. (*A*) Predicted distances between the donor (C_α of C108 on the exchanged cgRLC) and acceptor (2′/3′-O of nucleotide ribose), based on postpowerstroke (*Left*; PDB 1B7T, 8.9-nm magenta arrow) and prepowerstroke (*Right*; PDB 1DFL, 5.5-nm magenta arrow) structural models (similar to 2MYS and 1BR1, respectively). For simplicity, single-headed myosin S1 is depicted, although all experiments were performed on double-headed HMM. (*B*) Representative normalized fluorescence waveforms: instrument response (gray), donor only (black), Cy3-ADP (blue), Cy3-ADP + vanadate (burgundy), and nonlabeled HMM with bound Cy3-ATP acceptor (cyan). (*C*) M** (red) and M* (green) structural state obtained from the best-fit two structural state model of waveforms in *B*. (*D*) Mole fractions of M** (closed bars) and M* states (open bars) in *C* (n = 9, SEM). M.Cy3T (purple) from transient stopped-flow experiments in Fig. 2. Solutions contained 2 mM $MgCl_2$, 10 mM Tris (pH 7.5), 25 °C.

We measured TR-FRET of the labeled cardiac HMM (100 nM) with either bound Cy3-ADP (20 μM, saturating at equilibrium in a 100-μL cuvette), Cy3-ATP (2.0 μM, only after rapid mixing by stopped flow to avoid loss of bound Cy3-ATP via basal steady-state ATP turnover), or Cy3-ADP (2.0 μM, at equilibrium in a 100-μL cuvette) with excess vanadate (20 μM), all without actin (Fig. 1*B*), and then analyzed the resulting data as described in our previous publication (14) and in *SI Methods*. The TR-FRET decays (Fig. 1*B*) of the labeled cardiac myosin biosensor detect Cy3-ADP, Cy3-ATP, and Cy3-ADP.vanadate binding. FRET was greater, indicated by the average time constant for the measured time-resolved fluorescence waveforms, with saturating Cy3-ATP and Cy3-ADP.vanadate, compared with saturating Cy3-ADP. Thus, the average distance between the FRET probes is shorter in the presence of the ATP's γ-phosphate or γ-phosphate analog. We observed similar results in skeletal muscle myosin (14). TR-FRET waveforms can be modeled by well-defined structure-based functions (18) to determine if multiple interprobe distance distributions are present in the sample (*SI Methods* and Table S2)—multiple populations of distance distributions reflect structural heterogeneity in the sample. We performed this analysis as described in our previous studies (14) and validated the best-fit model based on χ^2 minimization (Fig. S2) and the geometry of the χ^2 error surface evaluated by parameter perturbation (Fig. S3) (14).

The TR-FRET waveforms were best fit by a model composed of two resolved structural states of the LCD (Fig. 1*C*), a short, 5.7-nm distance distribution and a longer 9.6-nm distance distribution. The centers of these distributions are consistent with the predictions from high-resolution crystal structures (Fig. 1*A*). The mole fraction of each distance distribution depended on the nucleotide binding state, just as we observed for skeletal myosin HMM (14). The mole fraction of the short-distance state (5.7 nm), termed M**, increased with Cy3-ATP binding or Cy3-ADP with excess vanadate (Fig. 1*D*) compared with Cy3-ADP alone. The apparent equilibrium constant ([M**]/[M*] at 25 °C) separating the M** and M* states under steady-state ATP bound conditions was 0.7—it is 4.0 in rabbit fast skeletal muscle HMM measured under similar thermodynamic conditions (14). The difference between the M**/M* equilibrium constant, under steady-state ATP bound conditions in the absence of actin, in skeletal muscle myosin HMM and bovine ventricular cardiac myosin HMM, is consistent with predictions of the ratio between prepowerstroke M** and postpowerstroke M* states, 0.8, made from tryptophan fluorescence measurements reported by Liu et al. (10).

As we observe in skeletal myosin (14), the short 5.7-nm distance M** state is also detected when Cy3-ADP is bound at saturation, although at a lower relative mole fraction (0.28; Fig. 1*D*). Thus, the average distance between probes is longer in the presence of ADP, and myosin spends a greater percentage of its time in a postrigor, postpowerstroke structural state, while still periodically isomerizing to a prepowerstroke state. This is consistent with crystallization studies showing that myosin can be crystalized in both prepowerstroke and postpowerstroke structural states in the presence of ADP (19). Together, these results demonstrate that the ventricular cardiac myosin LCD isomerizes between prepowerstroke and postpowerstroke orientations in the presence of both Cy3-ATP and Cy3-ADP and that the γ-phosphate shifts the apparent equilibrium constant for this isomerization at 25 °C from 0.4 with Cy3-ADP to 0.7 with Cy3-ATP and to 1.0 with Cy3-ADP.V_i.

OM Stabilizes an Actin-Attached Prepowerstroke Structural State. The FRET-based cardiac myosin biosensor allows us to correlate the structural kinetics of LCD rotation with the nucleotide binding

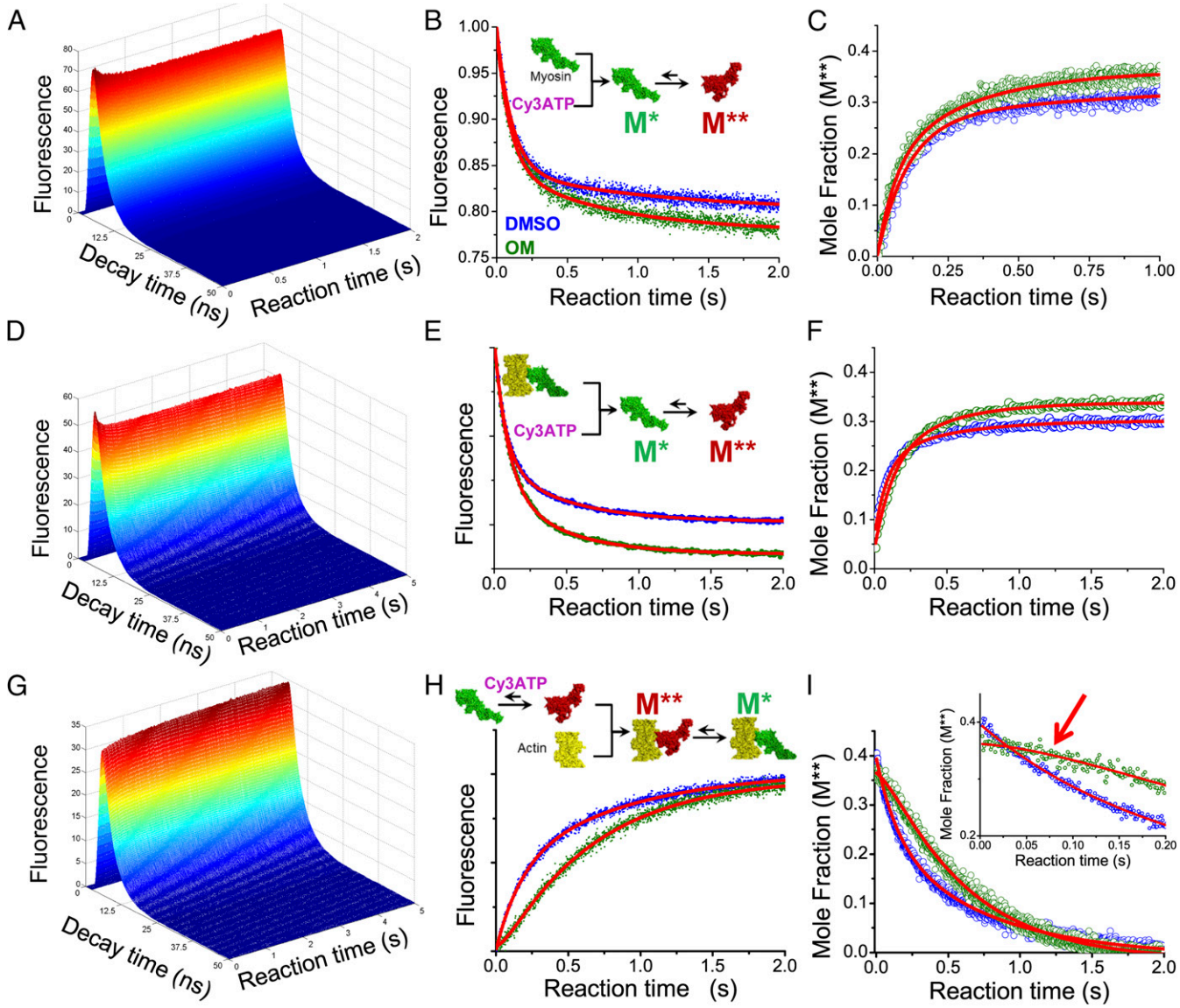

Fig. 2. $(TR)^2FRET$ used to detect actomyosin structural kinetics. (*A–C*) Cy3-ATP binding and approach to steady-state with donor-labeled cardiac HMM. Representative waveforms are shown in *A*, and total fluorescence is shown in *B*. Fits in *B* are as follows: $F_{DMSO} = 0.16e^{-9.4t} + 0.04e^{-0.9t} + 0.80$ and $F_{OM} = 0.14e^{-10.6t} + 0.07e^{-1.3t} + 0.78$. Mole fractions of the M** state are shown in *C*. Fits in *C* are as follows: $M^{**}_{DMSO} = 0.339 - 0.263e^{-9.2t} - 0.073e^{-1.03t}$ and $M^{**}_{OM} = 0.362 - 0.183e^{-15.2t} - 0.177e^{-3.13t}$. Experiments performed in the presence of 5 μM OM (green symbols) in assay buffer with 1% DMSO or DMSO alone (blue symbols). (*D–F*) Cy3-ATP binding to HMM as in *A*, in the presence of 20 μM actin. Total fluorescence is shown in *E*. Fits in *E* are as follows: $F_{DMSO} = 0.14e^{-13.4t} + 0.07e^{-2.2t} + 0.80$ and $F_{OM} = 0.16e^{-10.3t} + 0.08e^{-2.3t} + 0.77$. Mole fraction M** is shown in *F*. Fits in *F* are as follows: $M^{**}_{DMSO} = 0.301 - 0.155e^{-11.3t} - 0.15e^{-2.09t}$ and $M^{**}_{OM} = 0.338 - 0.181e^{-7.81t} - 0.116e^{-2.32t}$. (*G–I*) Powerstroke: TR-FRET waveforms starting from the steady state shown in *A*, after mixing with actin (40 μM postmix). Total fluorescence is shown in *H*, and mole fractions of M** are shown in *I*. *Inset* in *I* shows the lag phase induced by OM binding. $M^{**}_{DMSO} = 0.161e^{-6.72t} + 0.244e^{-1.37t}$ and $M^{**}_{OM} = 0.4469e^{-1.76t} - 0.069e^{-10.7t}$. TR-FRET waveforms in *A*, *C*, and *G* are acquired every 0.2 ms (1-ms average shown). Total fluorescence in *B*, *E*, and *H* is determined as described in *Supporting Information*. Mole fractions of M** structural states in *C*, *F*, and *I* are determined by fitting $(TR)^2FRET$ data obtained as in *A*, *D*, and *G*, to a global M*–M** structural state TR-FRET model described in *Supporting Information*. Solutions contained 2 mM $MgCl_2$, 10 mM Tris (pH 7.5), 1% DMSO, 25 °C. In the reaction schemes of *B*, *E*, and *H*, M** is depicting a fraction (Fig. 1*D*) of molecules in this state. Data are representative of $n = 9$ experiments.

state. We used a similar approach in our previous work to characterize ATP-induced priming of the prepowerstroke state in fast skeletal myosin II and the actin-induced powerstroke (14). We mixed cardiac HMM in the absence or presence of excess actin (20 μM) with varied [Cy3-ATP], all in the presence (5 μM in 1% DMSO) or absence (1% DMSO) of saturating OM and then acquired time-resolved FRET waveforms every 0.2 ms. These waveforms showed robust changes in the TR-FRET as evident by transient changes in their time-integrated total fluorescence (Fig. 2 *B* and *E*). We evaluated transient changes in the mole fraction of the M* and M** states (Fig. 2 *C* and *F*) determined by fitting the M*/M** structural state model described in Fig. 1 to the acquired data as performed in our previous work (14).

Cy3-ATP binding to HMM or HMM complexed with actin induced a biexponential time-dependent change in the total fluorescence (Fig. 2 *B* and *E*) of the AF488 donor probe and the M** mole fraction (Fig. 2 *C* and *F*) in the presence and absence of 5 μM OM, consistent with Cy3-ATP binding and formation of a high-FRET state described in Fig. 1. The rate constants for this biexponential transient increased with [Cy3-ATP] (Fig. 3 *A* and *B*), consistent with the characterized kinetics of cardiac myosins (20), and were not greatly affected by the drug. The apparent second-order rate

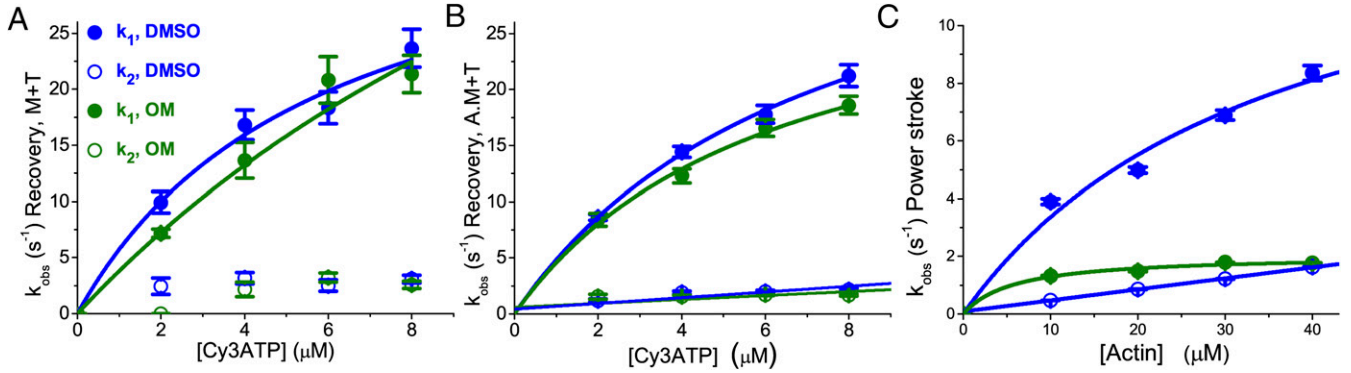

Fig. 3. Structural kinetics of ATP-driven actin detachment and actin-induced powerstroke. (*A*) Hyperbolic dependence between the rate constant for fast (closed circles) and slow (open circles) phases for Cy3-ATP induced M** accumulation during Cy3-ATP binding to HMM in 1% DMSO (blue) or 5.0 μM OM in 1% DMSO (green) performed in Fig. 2 *A–C*. Fits in *A* are as follows: $k_{1,DMSO}$ = 39 s^{-1} · [Cy3T]/(5.81 μM + [Cy3T]) and $k_{1,OM}$ = 75 s^{-1} · [Cy3T]/(18.7 μM + [Cy3T]). (*B*) Data acquired during Cy3-ATP binding to HMM complexed with 20 μM Actin performed in Fig. 2 *D–F*. Fits in *B* are as follows: $k_{1,DMSO}$ = 40.4 s^{-1} · [Cy3T]/(7.3 μM + [Cy3T]), $k_{1,OM}$ = 33.0 s^{-1} · [Cy3T]/(6.2 μM + [Cy3T]), $k_{2,DMSO}$ = 0.26 s^{-1}/μM · [Cy3T] + 0.42 μM, and $k_{2,OM}$ = 0.18 s^{-1}/μM · [Cy3T] + 0.59 μM. (*C*) Actin dependence of observed rate constants of the actin-induced powerstroke performed in Fig. 2 *G–I*. Fits in *C* are as follows: $k_{1,DMSO}$ = 15.3 s^{-1} · [Actin]/(35.5 μM + [Actin]), $k_{2,DMSO}$ = 0.038 s^{-1}/μM · [Actin] + 0.089 μM, and $k_{1,OM}$ = 2.05 s^{-1} · [Actin]/(5.85 μM + [Actin]). No fast phase is detected in the presence of OM. Solutions contained 2 mM $MgCl_2$, 10 mM Tris (pH 7.5), 25 °C.

constants for Cy3-ATP binding to HMM are 6.9 μM^{-1} s^{-1} and 4.0 μM^{-1} s^{-1} in the absence and presence of the drug, respectively, and to HMM complexed with actin, the constants are 4.0 μM^{-1} s^{-1} in both cases (Table S1; extrapolated from the hyperbolic [Cy3-ATP] dependence of the observed rate constants in Fig. 3). The total [M**] at steady-state in the absence of OM, extrapolated from the biexponential fit to the data, showed that the apparent M**/M* K_{eq} is 0.53 ± 0.03 in the absence of actin and 0.74 ± 0.04 in the presence of actin (20 μM). OM induces a small change in the M**/M* ratio, shifting the apparent K_{eq} to 0.56 ± 0.04 in the absence of actin and 0.87 ± 0.05 in the presence of actin (20 μM) (Fig. 2). This contrasts conclusions in previous work by Liu et al. (10). We address this contrast in the discussion.

OM Prevents the Actin-Induced Powerstroke. We measured actin-induced structural changes in the absence (1% DMSO) and presence of OM (5 μM in 1% DMSO) by preparing 0.2 μM AF488 labeled cardiac HMM with 2 μM excess Cy3-ATP in syringe A of the stopped flow, and then mixing this steady-state complex with varied concentrations of actin (10 to 40 μM, final concentrations after mixing) in syringe B containing 1 mM MgATP. The 1 mM MgATP prevents multiple actin-activated Cy3-ATP turnover reactions ensuring that the actin-induced changes in FRET (Fig. 2 *G–I*) reflect a single weak-to-strong actin-binding transition (21).

In the absence of OM, the total fluorescence transients (Fig. 2*H*) and M** mole fraction transients (Fig. 2*I*) were best fit by a biexponential function, consistent with a multistep kinetic process. The observed rate constant for the fast phase (Fig. 3*C*) increased hyperbolically with increasing [actin]. The $K_{0.5}$ for the hyperbolic dependence of the fast phase was 35.5 ± 18.1 μM, and the predicted maximum rate constant was 15.3 ± 4.3 s^{-1} (Table S1). OM induced a lag phase, followed by a single-exponential actin-activated powerstroke (Fig. 2 *I*, *Inset*, red arrow). This indicates that OM delays the actin-induced rotation of the LCD. The observed rate constant for the slow phase increased linearly with increasing [actin] (Fig. 3*C*) and did not exceed 2 s^{-1} at 40 μM actin. The slow phase is consistent with flux through actin-detached and weakly actin bound ATP hydrolysis reaction pathways (10, 22).

OM Uncouples the Powerstroke from Actin-Activated Phosphate Release. We compared the structural kinetics of the myosin powerstroke, described above, with the kinetics of actin-activated phosphate release (Fig. 4) using MDCC labeled phosphate binding protein (PBP) (22) as described in *SI Methods* and Fig. S4 and in our previous work (14). OM increased the actin-activated release of hydrolyzed phosphate (Fig. 4*B*), consistent with previous reports (5, 7). We ensured that the detected phosphate release was not affected by contaminating phosphate present in the actin by performing control experiments mixing the actin with ATP in the presence of the PBP sensor (Fig. S5). This is an important control because actin polymerization requires ATP, and even after phalloidin stabilization with extensive dialysis, polymerized actin can contain significant bound phosphate. We find that rapidly mixing actin by stopped flow can trigger release of the bound phosphate (Fig. S5), presumably reflecting sheering of longer filaments; thus, we extensively dialyze the stabilized actin in the presence of the phosphate mop to remove trace amounts of bound P_i.

The observed rate constant for actin-activated phosphate release increased hyperbolically with increasing [actin], exhibiting a $K_{0.5}$ of 15.5 ± 6.5 μM in the 1% DMSO and 26.1 ± 7.7 μM in the presence of 5 μM OM (Table S1). OM increased the maximum rate constant for actin-activated phosphate release from 11.6 ± 2.4 s^{-1} to 22.2 ± 3.9 s^{-1} (Table S1), consistent with previous reports (10) but in sharp contrast to the compound's effect on the powerstroke shown in (Fig. 2 *G–I*). Thus, OM binding to cardiac myosin inhibits the actin-induced rotation of the myosin light chain domain, despite

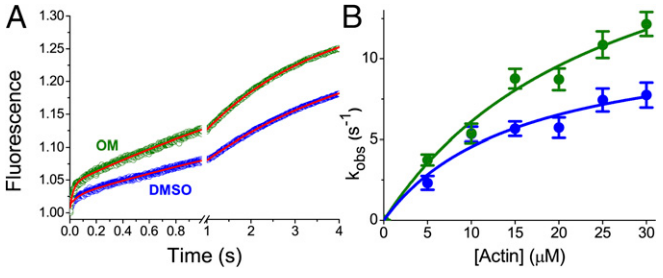

Fig. 4. Phosphate release kinetics in the presence and absence of OM. (*A*) Representative traces of P_i release detected by MDCC-PBP by sequential stopped-flow mixing of 1.0 μM unlabeled HMM with 2.0 μM ATP, aging the sample for 2.0 s, then mixing with 20 μM actin (final concentrations) and detecting for 20 s. $F_{OM} = 1.32 - 0.038e^{-21.9t} - 0.274e^{-0.36t}$ and $F_{DMSO} = 1.28 - 0.013e^{-13.2t} - 0.25e^{-0.24t}$. (*B*) The small-amplitude fast rate observed at each actin concentration, with and without OM. Solutions contained 10 μM MDCC-PBP, PiMOP (*SI Methods*), 2 mM $MgCl_2$, 10 mM Tris (pH 7.5), 1% DMSO 25 °C. Fits in *B* are as follows: $k_{obs,DMSO}$ = 11.6 s^{-1} [actin]/(15.5 μM + [actin]) and $k_{obs,OM}$ = 22.1 s^{-1} [actin]/(26.2 μM + [actin]), n = 9.

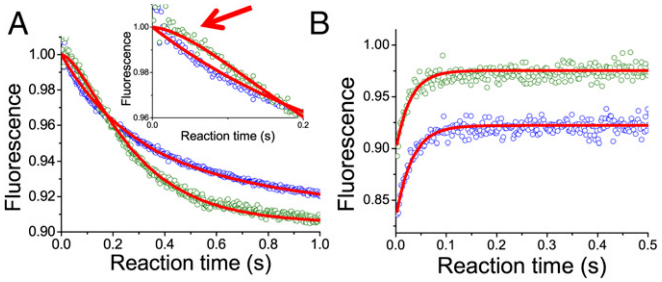

Fig. 5. Single actin-activated ATP turnover and ADP release kinetics in the presence of OM. (*A*) Actin-activated single turnover of mant-ATP performed by sequential mix of 1.0 μM HMM with 0.5 μM mant-ATP, aged 2 s and mixed with 20 μM actin and 1 mM ATP all in the presence or absence of saturating OM (postmix concentrations). Fits in *A* are as follows: $F_{DMSO} = 0.899 + 0.06e^{-3.9t} + 0.04e^{-0.71t}$ and $F_{OM} = 0.905 + 0.145e^{-4.4t} - 0.05e^{-12.1t}$. (*B*) ADP release kinetics measured by mixing 0.1 μM HMM bound to 10 μM actin and equilibrated with 2.0 μM Cy3-ADP mixed with 5.0 mM unlabeled ATP, in the presence or absence of saturating OM. Fits in *B* are as follows: $F_{DMSO} = 0.918 - 0.097e^{-31.5t}$ and $F_{OM} = 0.973 - 0.080e^{-35.1t}$.

activating actin-induced dissociation of phosphate from the myosin surface. This suggests that the compound increases the transition state free energy separating the prepowerstroke and postpowerstroke structural states of myosin and decreases the transition-state free energy for phosphate release.

OM Inhibits Actin-Activated ATP Turnover but Not ADP Release. OM's effect on the powerstroke suggests that single ATP turnover should be slowed. We investigated this by mixing 1.0 μM cardiac HMM with 0.5 μM 2′/3′-O-*N*-methylanthraniloyl adenosine 5′-triphosphate (mant-ATP), a fluorescent ATP derivative that reports bound ATP directly (21), in the stopped flow; aged the mixture for 2.0 s to allow hydrolysis; and then mixed the resulting steady-state with 20 μM actin similar to Fig. 2. Again, OM slowed ATP turnover in the first 100 ms of the reaction (Fig. 5), similar to the powerstroke. We verified that the single-turnover kinetics of mant-ATP and Cy3-ATP are identical (Fig. S6); thus, the FRET and mant-ATP turnover experiments are comparable. We measured the kinetics of ADP release by mixing an equilibrated solution of 10 μM actin, 0.1 μM of the AF488 labeled cardiac HMM, and 2.0 μM Cy3-ADP with 5.0 mM ATP (Fig. 5*B*) and then monitored the kinetics of Cy3-ADP dissociation by detecting FRET between the AF488 label and the Cy3 as in Fig. 2. The kinetics of the resulting fluorescence transients were indistinguishable from each other, exhibiting a single-exponential rate constant of 35.1 ± 2.2 s^{-1} in the presence of DMSO and 31.5 ± 1.5 s^{-1} in OM. Thus, OM does not alter the kinetics of ADP release, consistent with previous reports (4, 10).

OM Slows Light-Chain Domain Rotation in the Absence of ATP's γ-Phosphate. ADP binding stabilizes a small fraction of the M** structural state (Fig. 1). We investigated the effect of actin on this M** population by mixing an equilibrated solution of 0.1 μM AF488-labeled cardiac HMM and 1.0 μM Cy3-ADP with actin varied from 5.0 to 40 μM in the presence of 1 mM ATP. We acquired $(TR)^2$FRET waveforms as in Fig. 2 and then determined the mole fraction of M** and M* during the resulting transient. The M** mole fraction transients (Fig. 6*A*) were single-exponential. The rate constants for these exponentials increased hyperbolically with increasing [actin] (Fig. 6*B*). The $K_{0.5}$ for this increase was 4.7 ± 0.4 μM, and the k_{max} was 108.3 ± 4.6 s^{-1}, three times faster than the rate constant for ADP release detected in Fig. 5*B*. Thus, in the absence of OM, actin straightens the LCD before ADP is released from the ATPase site. We performed the same experiment in the presence of OM. The maximum rate constant for LCD rotation decreased to 4.1 ± 0.2 s^{-1}, a 26-fold decrease compared with the rate constant in the absence of the drug. Thus, OM inhibits LCD rotation, even in the absence of ATP's γ-phosphate.

OM Inhibits Actin-Induced LCD Rotation in the Presence of Both ADP and Vanadate. OM's acceleration of phosphate release suggests that it changes the energetics of myosin's actin activation. To further dissect the structural determinants for this acceleration, we evaluated the dependence of actin-induced LCD rotation on orthovanadate (V_i), a phosphate analog that binds with submicromolar affinity to myosin in the presence of ADP, and μM affinity in the presence of saturating actin and ADP. Vanadate binding stabilizes a closed structural state of the switch-2 and switch-1 loops thought to mimic a posthydrolysis/prephosphate release structural configuration (23). In our previous work investigating the powerstroke and phosphate release in skeletal myosin, we found that vanadate binding to myosin with ADP ($ADP.V_i$) prevented LCD rotation, even though LCD rotation preceded phosphate release during single ATP turnover. Thus, vanadate binding traps a locked structural state of myosin where the LCD is prevented from rotating. We propose that this trapped state precedes the movement of phosphate away from ADP after hydrolysis, consistent with arguments proposed by Llinas et al. (19). We hypothesized that OM would slow the actin-activated exchange of vanadate, just as it slows actin-activated LCD rotation, given our prior hypothesized coupling between switch-2 movement and the powerstroke in skeletal myosin.

We measured the ability of vanadate to prevent the actin-induced rotation of the cardiac myosin LCD, by performing $(TR)^2$FRET experiments mixing 0.1 μM AF488-labeled cardiac HMM, 2.0 μM Cy3-ADP, and 100 μM vanadate with a range of actin concentrations all containing 5.0 mM ATP. We acquired and fit the resulting waveforms as described for Fig. 2. In the absence and presence of OM, the M** mole fraction transients were single-exponential with the rate constants increasing hyperbolically with increasing actin (Fig. 6). At 100 μM vanadate, the k_{max} decreased from 0.010 ±

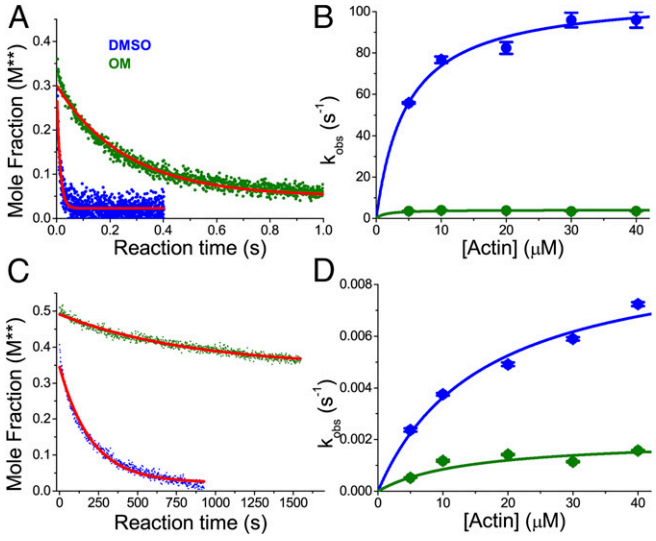

Fig. 6. OM inhibits actin-induced LCD rotation when Cy3-ADP or Cy3-ADP and vanadate are bound to HMM. (*A*) 0.1 μM labeled HMM and 2.0 μM Cy3-ADP were equilibrated and then mixed with 20 μM actin and 5 mM ATP in the presence (green) or absence (blue) of 10 μM OM. (*B*) Actin dependence of the observed rate constant obtained by fitting data in *A* to a single-exponential function over a range of actin concentrations. $k_{obs,DMSO} = 108.3\ s^{-1}$ [Actin]/(4.6 μM + [Actin]) and $k_{obs,OM} = 4.1\ s^{-1}$ [Actin]/(0.7 μM + [Actin]). (*C*) 0.1 μM HMM, 2.0 μM Cy3-ADP, and 100 μM vanadate were equilibrated for 20 min and then mixed with 20 μM actin, 100 μM vanadate, and 5 mM ATP. (*D*) Actin dependence of the observed rate constant obtained by fitting data in *D* to a single hyperbolic function. $k_{obs,DMSO} = 9.5 \times 10^{-3}\ s^{-1}$/(16.2 μM + [Actin]) and $k_{obs,OM} = 2.03 \times 10^{-3}\ s^{-1}$/(14.0 μM + [Actin]).

$0.001\ s^{-1}$ in the absence of OM to $0.002 \pm 0.001\ s^{-1}$ in the presence of the drug, a fivefold decrease, whereas the [actin] $K_{0.5}$ did not change (16.2 ± 3.9 μM and 14.0 ± 4.6 μM, respectively). Thus, OM slows actin-induced vanadate exchange but does not change the affinity of actin for myosin.ADP.V_i.

The observed rate constant for actin-activated dissociation of Cy3-ADP.Vi decreases with increasing vanadate, indicating that rebinding of vanadate to actomyosin.ADP before ADP dissociation traps the complex. The [vanadate] dependence of this inhibition reflects the affinity of actomyosin.ADP for vanadate. We varied the concentration of vanadate included in the reaction (Fig. S7*C*), fit the resulting M** transients to single-exponential functions as in Fig. 6, and then evaluated the dependence of the observed rate constant on [V_i] (Fig. S7*C*). The maximum rate constant determined from these fits (as [V_i] goes to 0 μM) was $85.5 \pm 1.9\ s^{-1}$ in the absence of OM and $8.7 \pm 3.4\ s^{-1}$ in the presence of the drug, consistent with the observed rate constant in the presence of ADP without vanadate under similar [actin] conditions (Fig. 6*B*). The $K_{0.5}$ for this dependence was 3.8 ± 0.1 μM in the absence of OM and 2.7 ± 1.8 μM in the presence of the drug. Thus, OM does not change the affinity of actomyosin.ADP for vanadate; it only slows exchange of vanadate with actomyosin.ADP, in contrast to OM's acceleration of phosphate release. We discuss these differences below.

Discussion

In this study, we investigated how OM alters the structural kinetics of bovine ventricular cardiac myosin's force-transducing structural transition, actin-induced light chain domain rotation—vis-à-vis the powerstroke. Previous kinetic studies showed that OM inhibits cardiac myosin's basal and actin-activated ATPase activity, while simultaneously increasing the apparent rate constant for actin-induced phosphate release twofold to threefold (4, 10). OM also shifts the equilibrium constant for hydrolysis toward the post-hydrolysis ADP.P_i state by more than sixfold. However, those studies do not determine which step in the ATPase cycle is slowed by the drug in vitro, because the measured biochemical steps are either affected to a negligible degree or are accelerated by OM (10); none yet examined are greatly slowed.

OM dramatically alters myosin's mechanical properties. The drug inhibits the sliding velocity of actin filaments in vitro more than 20-fold (7, 10, 24), while simultaneously increasing the ensemble stall force induced by a model for viscoelastic load in the same motility assay (7). Aksel et al. suggested that OM increases the relative amount of time that myosin spends bound to actin during its ATPase cycle in vitro as much as 10-fold and increased the average force generated by actin-attached cross-bridges (7), suggesting that it increases the unimolecular force-generating capacity of single myosin molecules and the actin-binding affinity of cardiac myosin or cardiac myosin bound by ADP (25–27).

Myocardial mechanics studies reached similar conclusions (11), showing that OM increases the fraction of time cardiac myosin spends attached to actin generating force, although not nearly as much as predicted from in vitro motility studies (7, 10, 24). This increase, which occurred in both mouse, enriched in the faster α-cardiac myosin isoform, and human ventricular myocardium, highly enriched in the slower β-cardiac myosin isoform, is primarily the result of a decrease in the rate constant for actin detachment (11). The kinetic step that limits actin detachment in these experiments was not clear, because the kinetics of ADP release in the absence of load is not altered by OM in solution (Fig. 5) (10). Future work will be needed to determine whether OM slows ADP release when myosin is loaded. Our results, showing a 25-fold decrease in the rate of actin-induced LCD rotation when ADP is bound in the presence of OM (Fig. 6), suggest that it will. They also suggest that in the presence of OM, the rate limiting step for steady-state ATPase cycling and for force development in the contracting heart is actin-induced rotation of the cardiac myosin LCD (Fig. 7).

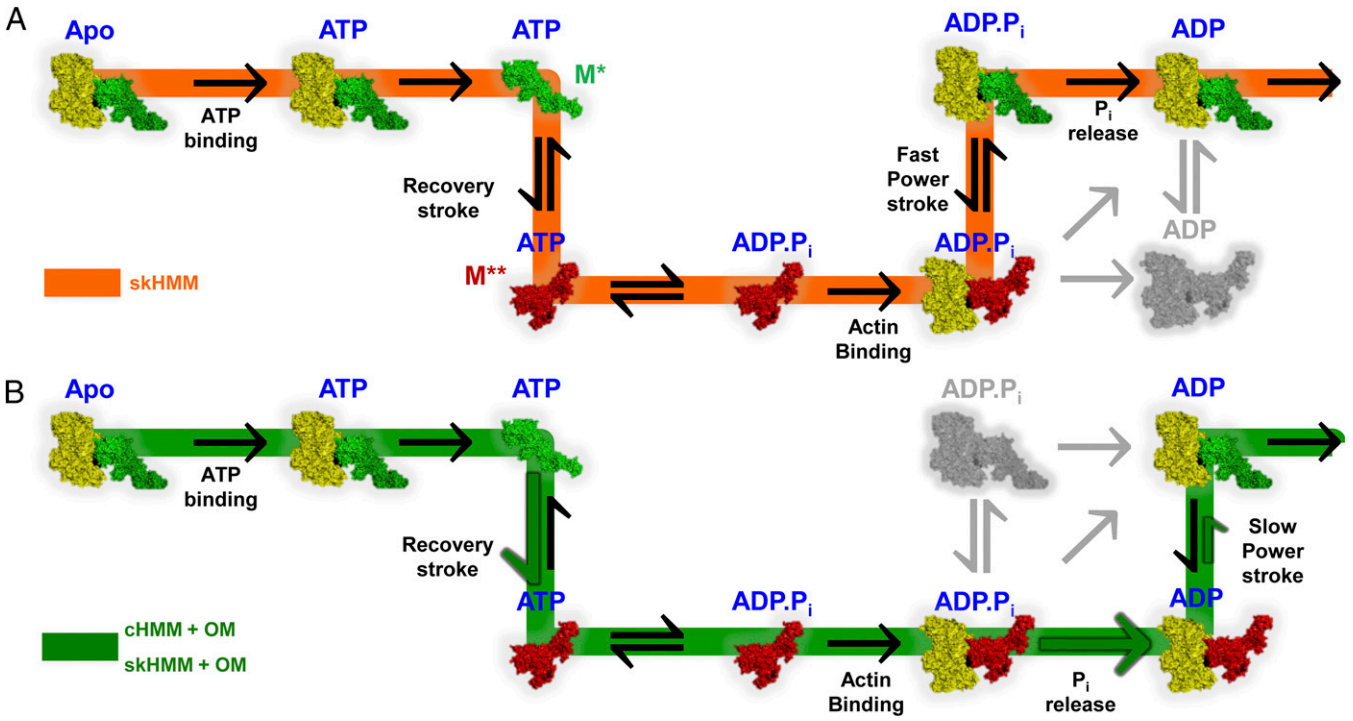

Fig. 7. Thermodynamic models for modulation of P_i release–powerstroke coupling by OM. (*A*) The coordination of the powerstroke and P_i release in skeletal HMM (skHMM) is best fit by a powerstroke first model (orange) (14). (*B*) However, cardiac HMM (cHMM) + OM and skHMM + OM accelerates P_i release and stabilizes the M** state, whereas introducing a lag in the powerstroke (green arrows) suggesting a phosphate-first mechanism (green line). In each case, statistical mechanics requires that off-pathway states are accessible (gray).

OM also binds to skeletal myosin and inhibits the steady-state ATPase cycling (Fig. S8), albeit at higher concentrations of the drug (4). Thus, we performed similar experiments with a skeletal myosin HMM and find that OM slows the powerstroke there as well (Fig. S8 and *SI Methods*). This suggests that derivatives of OM that specifically bind other myosin family members—fast skeletal myosin; smooth and nonmuscle myosin II; or transport motors like myosin V, VI, VII, or X—at submicrometer concentrations would be potent modulators of their unique mechanoenzymologies and molecular physiology in cells.

OM Slows the Powerstroke but Accelerates Phosphate Release. When we began this study, we hypothesized that OM accelerates the powerstroke as it accelerates phosphate release (Fig. 4 and Table S1) (4, 10). Our work on fast skeletal myosin II (14), *Dictyostelium disodium* myosin II (13), and myosin V (15) shows that FRET-detected structural transitions associated with lever arm rotation occur faster than the actin-induced dissociation of hydrolyzed phosphate. Thus, we reasoned that OM's acceleration of P_i release would be accompanied by a corresponding acceleration in the powerstroke.

In the absence of OM, the observed phosphate release rate constant predicted from fitting the actin dependence of the fast phase of actin-induced phosphate dissociation from the myosin surface is 25% slower than the predicted maximum rate constant for light chain domain rotation detected by FRET (11.6 s^{-1} vs. 15.5 s^{-1}; Table S1). This 25% difference is comparable to the 43% difference seen in myosin V, where phosphate release is 201 s^{-1} and lever arm rotation is 352 s^{-1} (15), but much less than the 10-fold difference observed in fast skeletal myosin HMM, where phosphate release was measured at 38 s^{-1} and LCD rotation was measured at >500 s^{-1} (14), and in the *Dictyostelium* myosin II catalytic domain, where phosphate release was 37 s^{-1} and relay helix straightening was >500 s^{-1} (13).

OM increased the rate constant for actin-activated phosphate release from 11.6 ± 2.4 s^{-1} to 22.1 ± 3.9 s^{-1}; a similar change was observed by Liu et al. (10). However, rather than accelerate the powerstroke as we initially hypothesized, OM causes the force-generating lever arm rotation to lag behind actin-activated phosphate release (Fig. 2 *H* and *I*). The preexponential amplitude of the lag increased hyperbolically with [OM] (Fig. S9 and *SI Methods*). The apparent $K_{0.5}$ for this increase was 25 μM (Fig. S9) compared with the reported affinity of OM binding to cardiac myosin alone, 1.6 μM (4). This suggests that OM binds more weakly to the actomyosin.ADP complex than to myosin in the absence of actin. This is reminiscent of how actin affects the affinity of myosin II for blebbistatin (28) and for vanadate in the presence of ADP (14) and is consistent with the stabilization of an actin-bound prepowerstroke structural state. Furthermore, OM dramatically slowed actin-induced LCD rotation in our cardiac HMM sensor with either bound ADP or bound ADP.V_i (Fig. 6). This inhibited rotation precedes ADP release because OM has no effect on the kinetics of ADP dissociation from cardiac HMM bound to actin (Fig. 5*B*). Thus, OM's primary effect is to inhibit the actin-induced rotation of cardiac myosin's light chain domain before and after phosphate dissociation.

The crystal structure of the catalytic domain of human cardiac myosin lacking light chains, crystalized in a nucleotide-free, near-rigor/prerecovery/postpowerstroke-like structural state, in the presence of OM (5), suggests that OM increases the twist of myosin's critical β-sheet in the absence of nucleotide. The structure of cardiac myosin in a true prepowerstroke state with bound OM has not been reported. Such a state, when revealed, will provide key insight into OM's mode of action. The subtle twisting of the β-sheet by OM (5) is consistent with the slight stabilization of the prepowerstroke state shown in Fig. 2 and Fig. S7: the β-sheet is hypothesized to twist with ATP binding and subsequent closure of myosin's conserved nucleotide binding loops—switch-1, switch-2, and the P-loop. The powerstroke structural transition is coupled to the structural state of these conserved nucleotide-binding elements and is hypothesized to correlate with β-sheet straightening, although the exact timing of this coordination has not been fully established.

OM Increases the Fraction of Time That Cardiac Myosin Spends Bound to Actin. Phosphate release is coupled to the weak-to-strong actin-binding transition. Dissociation of hydrolyzed phosphate allows the actin-binding cleft to close, switch-I to open, and Mg^{+2} and ADP to dissociate (6). OM accelerates P_i release (4, 10), but as Fig. 2*I* shows, it slows down the powerstroke while having no effect on ADP release (Fig. 5). These changes would increase the amount of time that individual myosin cross-bridges spend bound to actin, consistent with cardiac myocardium experiments suggesting a 50% increase in the strong actin-binding attachment time, a 20% increase in force-generating cross-bridge stiffness and a corresponding increase in cross-bridge mediated thin-filament activation (11).

The inhibition of the powerstroke by OM helps explain the decreased actin sliding velocity seen in the in vitro motility assay (7, 10, 24). The powerstroke performs mechanical work on actin to drive filament sliding. OM inhibits powerstroke rotation, prolonging the time myosin spends bound to actin in a prepowerstroke state after phosphate dissociates. This state binds actin more strongly than before phosphate is released as indicated by comparing the $K_{0.5}$ values for the [actin]-dependent transitions measured in this study (Table S1), all of which decrease in the absence of P_i or P_i analogs. Thus, the OM trapped prepowerstroke state should act as a drag force on actin filament sliding, just as seen in the in vitro motility assay (7, 10, 24).

OM lowered the [actin] $K_{0.5}$ for the actin-induced powerstroke from 35 to 5μM and for actin-induced LCD rotation in the presence of ADP from 5 to 0.7 μM (Table S1), all indicating that the drug strengthens the affinity of cardiac myosin binding to actin during force generation. This strengthened binding is consistent with a previously proposed increase in the actomyosin duty cycle (7, 10, 24) during ATPase cycling and also with the observed increase in maximum ensemble force generation in the in vitro motility assay (7) because maximum force generation by myosins correlates with the energetics of actomyosin binding (25–27).

However, OM does not strengthen the actin binding affinity of ADP.phosphate-bound cardiac myosin. The [actin] $K_{0.5}$ for exchange of ADP and vanadate, a kinetically stable posthydrolysis ADP.P_i analog, was 16.2 and 14.0 μM in the absence and presence of OM, respectively (Table S1), whereas the [actin] $K_{0.5}$ for actin-activated phosphate release was increased from 15.5 to 26.2 μM (Table S1). The difference between the [actin] $K_{0.5}$ for myosin.ADP.V_i and the [actin] $K_{0.5}$ for phosphate release in the presence of OM suggests that myosin is in unique structural states under the two biochemical conditions (P_i vs. V_i) consistent with OM's acceleration of actin-activated phosphate dissociation from the myosin surface and slowed actin-induced vanadate exchange.

The actin-activated ATPase K_m decreases twofold with OM binding (Table S1); this, together with the decreased actin $K_{0.5}$ for LCD rotation after phosphate release and during actin-induced LCD rotation in the presence of ADP, suggests that strong actin-binding postphosphate release species accumulate on actin during steady-state ATPase cycling. Consistent with this, the M** mole fraction is increased at steady-state upon mixing cardiac HMM bound to actin with excess Cy3-ATP in Fig. 2.

The Cardiac Myosin Powerstroke Is Closely Coordinated with Phosphate Release in the Absence of OM. Our previous studies of fast skeletal myosin showed that actin induces LCD rotation more than 10 times faster than phosphate, dissociating from the surface of myosin, is detected in solution using a fluorescent phosphate binding protein phosphate sensor (14). In that same study, we found that LCD rotation is blocked by both blebbistatin and vanadate.

Both molecules are thought to trap phosphate in the nucleotide binding site with the switch-2 loop closed (23, 29). Together, these results suggest that switch-2 opening is required for LCD rotation, phosphate release, and the weak-to-strong actin binding transition and that actin initiates both phosphate release and the powerstroke by changing the dynamics of switch-2.

Phosphate release and the powerstroke are definable molecular events. The simplest thermodynamic mechanism explaining the coordination between these events is depicted in Fig. 7. Statistical mechanics requires that the molecules of the system diffuse over all possible paths in this mechanism—some myosin molecules will dissociate phosphate before the powerstroke (Fig. 7*B*); others will undergo the powerstroke before phosphate release (Fig. 7*A*); and some will undergo both transitions simultaneously, traversing the landscape diagonally from the prepowerstroke ADP.P_i state to the postpowerstroke ADP state.

In skeletal myosin, it is clear that the structural transition associated with LCD rotation precedes phosphate dissociation in solution, and thus, the orange pathway in Fig. 7*A* is favored. In cardiac myosin, our results show that at saturating [actin] the powerstroke occurs only 0.25 times faster than phosphate release (Table S1). This difference is similar to the 0.43-fold difference seen in myosin V and suggests that LCD rotation is more closely coordinated with actin-induced phosphate release in higher-duty ratio motors, like β-cardiac myosin and myosin V, than in low-duty ratio motors like skeletal muscle myosin. The physiological implications for the difference between the coordination of the powerstroke and phosphate release in different myosin isoforms remain to be fully determined but probably reflects the intrinsic role each protein plays in cells.

OM Increases the Transition State Free Energy for the Powerstroke. OM is an allosteric inhibitor of myosin ATPase cycling (10). It is also an allosteric activator of phosphate release (5, 10) and of maximum force generation (7, 11). Our results show that OM binding induces small changes in the distribution of M* and M** states in the absence of actin (Fig. 2*C*). This is not what we expected based on the change in the apparent K_{eq} for ATP hydrolysis measured by Liu et al. (10). That study made two important predictions: (*i*) In ventricular cardiac myosin, LCD orientation, as inferred from tryptophan fluorescence—a proxy for the M** state in most myosins (30)—is not tightly coupled to hydrolysis. (*ii*) OM binding causes a large change in the M**/M* K_{eq} as indicated by its effect on tryptophan fluorescence. In that study, OM binding shifts the apparent K_{eq} for the hydrolysis of ATP by myosin from 2.7 to 6.8, while it shifts the apparent M**/M* K_{eq} estimated from tryptophane fluorescence, from 0.77 to 3.98 (10). Our FRET measurements show a much smaller change in the K_{eq} for LCD priming, 0.52–0.56 in the absence of actin (Fig. 2), and 0.74–0.87 in the presence of actin—essentially no change, much less than predicted by Liu et al. (10). The Eyring–Polanyi transition state model (31) predicts these changes in K_{eq} should not alter the ms-resolved kinetics of the protein.

The dramatic effect that OM has on the kinetics of the powerstroke structural transition, in the presence of ATP (Fig. 2), ADP (Fig. 6*A*), and ADP.V_i (Fig. 6*C*), shows that the primary effect of the compound on the LCD is to increase the transition-state Gibbs free energy separating the prepowerstroke and postpowerstroke orientations of the LCD, most notably when bound to actin, after phosphate dissociates. In the high-resolution structure published by Winkelmann et al. (5), OM makes important contacts with multiple structural elements that move with respect to one another during the powerstroke, and thus, by binding these elements, OM should slow or even prevent LCD rotation, just as we observe.

Conclusions

We have investigated the actin-induced structural kinetics of cardiac myosin's light chain domain during the powerstroke to determine how OM modulates the coordination between the phosphate release biochemical step and the force-generating rotation of the myosin LCD. Our results reveal a previously unknown aspect of OM's mode of action: the small-molecular therapeutic changes the coordination between phosphate release and the powerstroke and inhibits the powerstroke by increasing the transition-state free energy for actin-induced LCD rotation. These results provide molecular insight into OM's diverse range of effects in patients and in vitro biochemical studies.

Methods

Protein Purification and Labeling. Bovine ventricular cardiac myosin was purified based on procedures modified from Margossian and Lowey (32) and described in detail in *Supporting Information*. Purified HMM was generated by α-chymotrypsin digestion, stopped by addition of pefabloc (*Roche*), and then isolated by chromatography as described in *Supporting Information*. The chicken gizzard smooth muscle myosin regulatory light chain was expressed, purified, labeled, and exchanged as described in our previous work (14) with modifications described in *Supporting Information*. Actin was purified from rabbit skeletal muscle by acetone dehydration followed by extraction into ice cold water, described in detail in *Supporting Information*.

Spectroscopy. Time-resolved FRET experiments were carried out as described in our previous studies (14) explained in detail in *Supporting Information*.

Transient Kinetics. Stopped-flow experiments were performed on a Biologic SFM-20 equipped with a transient TRF spectrophotometer, described in our previous work (14). Sequential mix experiments were performed on an Applied Photophysics sequential mix stopped flow.

ACKNOWLEDGMENTS. We thank John Lipscomb for use of his sequential stopped-flow instrument. We thank Anne Houdusse for generous communications, Josh Baker and Travis Steward for sharing their cardiac myosin purification procedure (which we modified for the experiments presented here), and Piyali Guhathakurta for expert assistance in the purification of the cardiac myosin used in this work. This study was supported by grants from the American Heart Association (14SDG20480032 to J.M.M.) and from NIH (R01AR32961 and R42DA037622 to D.D.T.). J.A.R. was supported by a Graduate Excellence Fellowship from the University of Minnesota.

1. Mozaffarian D, et al.; Writing Group Members; American Heart Association Statistics Committee; Stroke Statistics Subcommittee (2016) Heart disease and stroke statistics—2016 update: A report from the American Heart Association. *Circulation* 133(4): e38–e360.
2. Fonarow GC, et al.; OPTIMIZE-HF Investigators and Hospitals (2007) Characteristics, treatments, and outcomes of patients with preserved systolic function hospitalized for heart failure: A report from the OPTIMIZE-HF Registry. *J Am Coll Cardiol* 50(8): 768–777.
3. Solaro RJ, Tardiff JC (2013) *Biophysics of the Failing Heart: Physics and Biology of Heart Muscle* (Springer, New York).
4. Malik FI, et al. (2011) Cardiac myosin activation: A potential therapeutic approach for systolic heart failure. *Science* 331(6023):1439–1443.
5. Winkelmann DA, Forgacs E, Miller MT, Stock AM (2015) Structural basis for drug-induced allosteric changes to human β-cardiac myosin motor activity. *Nat Commun* 6:7974.
6. Sweeney HL, Houdusse A (2010) Structural and functional insights into the Myosin motor mechanism. *Annu Rev Biophys* 39:539–557.
7. Aksel T, Choe Yu E, Sutton S, Ruppel KM, Spudich JA (2015) Ensemble force changes that result from human cardiac myosin mutations and a small-molecule effector. *Cell Reports* 11(6):910–920.
8. Cleland JG, et al. (2011) The effects of the cardiac myosin activator, omecamtiv mecarbil, on cardiac function in systolic heart failure: A double-blind, placebo-controlled, crossover, dose-ranging phase 2 trial. *Lancet* 378(9792):676–683.
9. Greenberg BH, et al. (2015) Safety and tolerability of omecamtiv mecarbil during exercise in patients with ischemic cardiomyopathy and angina. *JACC Heart Fail* 3(1):22–29.
10. Liu Y, White HD, Belknap B, Winkelmann DA, Forgacs E (2015) Omecamtiv Mecarbil modulates the kinetic and motile properties of porcine β-cardiac myosin. *Biochemistry* 54(10):1963–1975.
11. Mamidi R, Gresham KS, Li A, dos Remedios CG, Stelzer JE (2015) Molecular effects of the myosin activator omecamtiv mecarbil on contractile properties of skinned myocardium lacking cardiac myosin binding protein-C. *J Mol Cell Cardiol* 85:262–272.
12. Nesmelov YE, et al. (2011) Structural kinetics of myosin by transient time-resolved FRET. *Proc Natl Acad Sci USA* 108(5):1891–1896.

13. Muretta JM, Petersen KJ, Thomas DD (2013) Direct real-time detection of the actin-activated power stroke within the myosin catalytic domain. *Proc Natl Acad Sci USA* 110(18):7211–7216.
14. Muretta JM, Rohde JA, Johnsrud DO, Cornea S, Thomas DD (2015) Direct real-time detection of the structural and biochemical events in the myosin power stroke. *Proc Natl Acad Sci USA* 112(46):14272–14277.
15. Trivedi DV, et al. (2015) Direct measurements of the coordination of lever arm swing and the catalytic cycle in myosin V. *Proc Natl Acad Sci USA* 112(47): 14593–14598.
16. Muretta JM, et al. (2013) Loop L5 assumes three distinct orientations during the ATPase cycle of the mitotic kinesin Eg5: A transient and time-resolved fluorescence study. *J Biol Chem* 288(48):34839–34849.
17. Muretta JM, et al. (2015) The structural kinetics of switch-1 and the neck linker explain the functions of kinesin-1 and Eg5. *Proc Natl Acad Sci USA* 112(48): E6606–E6613.
18. Lakowicz JR (2006) *Principles of Fluorescent Spectroscopy* (Springer, New York), 3rd Ed.
19. Llinas P, et al. (2015) How actin initiates the motor activity of Myosin. *Dev Cell* 33(4): 401–412.
20. Deacon JC, Bloemink MJ, Rezavandi H, Geeves MA, Leinwand LA (2012) Identification of functional differences between recombinant human α and β cardiac myosin motors. *Cell Mol Life Sci* 69(13):2261–2277.
21. De La Cruz EM, Ostap EM (2009) Kinetic and equilibrium analysis of the myosin ATPase. *Methods Enzymol* 455:157–192.
22. White HD, Belknap B, Webb MR (1997) Kinetics of nucleoside triphosphate cleavage and phosphate release steps by associated rabbit skeletal actomyosin, measured using a novel fluorescent probe for phosphate. *Biochemistry* 36(39):11828–11836.
23. Smith CA, Rayment I (1996) X-ray structure of the magnesium(II).ADP.vanadate complex of the Dictyostelium discoideum myosin motor domain to 1.9 A resolution. *Biochemistry* 35(17):5404–5417.
24. Wang Y, Ajtai K, Burghardt TP (2014) Analytical comparison of natural and pharmaceutical ventricular myosin activators. *Biochemistry* 53(32):5298–5306.
25. Baker JE, Thomas DD (2000) A thermodynamic muscle model and a chemical basis for A.V. Hill's muscle equation. *J Muscle Res Cell Motil* 21(4):335–344.
26. Baker JE, Thomas DD (2000) Thermodynamics and kinetics of a molecular motor ensemble. *Biophys J* 79(4):1731–1736.
27. Karatzaferi C, Chinn MK, Cooke R (2004) The force exerted by a muscle cross-bridge depends directly on the strength of the actomyosin bond. *Biophys J* 87(4):2532–2544.
28. Kovács M, Tóth J, Hetényi C, Málnási-Csizmadia A, Sellers JR (2004) Mechanism of blebbistatin inhibition of myosin II. *J Biol Chem* 279(34):35557–35563.
29. Allingham JS, Smith R, Rayment I (2005) The structural basis of blebbistatin inhibition and specificity for myosin II. *Nat Struct Mol Biol* 12(4):378–379.
30. Málnási-Csizmadia A, Woolley RJ, Bagshaw CR (2000) Resolution of conformational states of Dictyostelium myosin II motor domain using tryptophan (W501) mutants: Implications for the open-closed transition identified by crystallography. *Biochemistry* 39(51):16135–16146.
31. Eyring H (1935) The activated complex in chemical reactions. *J Chem Phys* 3(2):107–115.
32. Margossian SS, Lowey S (1982) Preparation of myosin and its subfragments from rabbit skeletal muscle. *Methods Enzymol* 85(Pt B):55–71.